On the Accessibility of Higher-*n* Phases in Formamidinium-Based Ruddlesden-Popper and Dion–Jacobson Layered Hybrid Perovskites

Ghewa AlSabeh, Vladislav Slama, Masaud Almalki, Lena Merten, Paul Zimmermann, Alexander Hinderhofer, Pascal Alexander Schouwink, Virginia Carnevali, Nikolaos Lempesis, Lorenzo Agosta, Frank Schreiber, Ursula Rothlisberger, Michael Grätzel,* and Jovana V. Milić**

Layered (2D) hybrid perovskites offer a promising alternative for stabilizing halide perovskite materials, with a growing interest in formamidinium (FA^+) lead iodide derivatives for photovoltaics due to their exceptional optoelectronic properties. While their potential increases with the number of inorganic layers (*n*), the experimental evidence suggests that obtaining $n > 2$ phases is challenging for FA-based layered perovskites. To address this challenge and identify the conditions governing the formation of higher-*n* phases, representative FA-based layered hybrid perovskite materials containing aromatic spacer cations, namely benzylammonium (BNA) and 1,4-phenylenedimethanammonium (PDMA)—are investigated as model systems for the corresponding Ruddlesden-Popper and Dion-Jacobson phases based on $(BNA)_2FA_{n-1}Pb_nI_{3n+1}$ and $(PDMA)FA_{n-1}Pb_nI_{3n+1}$ formulations ($n = 1$–3), respectively. Moreover, the effect of Cs^+ cations on the formation of $n > 1$ phases is explored through a combination of X-ray scattering measurements, solid-state NMR spectroscopy, optoelectronic characterization, and density functional theory calculations. Despite improved photovoltaic performances, the formation of higher ($n > 2$) phases is excluded, even in the presence of Cs^+, due to the favorable formation of other low-dimensional phases revealed by the theoretical investigation. The results contribute to a comprehensive understanding of these materials of broad interest to their application in optoelectronics.

1. Introduction

Hybrid halide perovskites represent mixed ionic-electronic semiconductors with high absorption coefficients, long charge carrier lifetimes and diffusion lengths, and exceptional defect tolerance.[1,2] These properties have established hybrid halide perovskites as attractive semiconductors in photovoltaics, light-emitting diodes, photodetectors, and the emerging field of optoionics.[1–5] Despite their outstanding performances, perovskite devices have not been commercialized due to their limited stability when exposed to oxygen, moisture, temperature variations, light, and voltage bias.[2,6–8] As a result, a growing interest in low-dimensional (2D) or layered hybrid perovskites (LHPs) has emerged due to their superior stability.[9–12] They are based on layers of organic ammonium cations templating hybrid perovskite layers[9,13] whose stability is attributed to the hydrophobicity of the organic spacers and their ability to mitigate ion

---

G. AlSabeh, J. V. Milić
Adolphe Merkle Institute
University of Fribourg
Fribourg 1700, Switzerland
E-mail: jovana.milic@unifr.ch

The ORCID identification number(s) for the author(s) of this article can be found under https://doi.org/10.1002/aelm.202500164

DOI: 10.1002/aelm.202500164

G. AlSabeh, V. Slama, M. Almalki, P. A. Schouwink, V. Carnevali, N. Lempesis, L. Agosta, U. Rothlisberger, M. Grätzel
Institute of Chemical Sciences and Engineering
School of Basic Sciences
Ecole Polytechnique Fédérale de Lausanne
Lausanne CH-1015, Switzerland
E-mail: ursula.roethlisberger@epfl.ch; michael.graetzel@epfl.ch

M. Almalki
Future Energy Technology Institute
King Abdulaziz City for Science and Technology
Riyadh 11442, Saudi Arabia

L. Merten, P. Zimmermann, A. Hinderhofer, F. Schreiber
Institut für Angewandte Physik
Universität Tübingen
72076 Tübingen, Germany

migration.[13–17] They can be defined by the $S_xA_{n\text{-}1}M_nX_{3n+1}$ formula where S is the spacer with ammonium-functionalized groups (x = 2, if the cation is monofunctional, or x = 1, if it is bifunctional), A stands for the central monovalent cations (e.g., methylammonium (MA^+), formamidinium (FA^+), or Cs^+), M represents divalent metal cations (mostly Pb^{2+}, Sn^{2+}), and X halide anions (I^-, Br^-, Cl^-), whereas n defines the number of perovskite layers.[9,18] The structures are classified into Ruddlesden–Popper (RP) and Dion–Jacobson (DJ) phases in which each has a different relative orientation of the adjacent perovskite layers.[18] The inorganic slabs displaced by half a unit cell along the in-plane directions is a characteristic of RP phases, usually containing a bilayer of monofunctional spacers,[19] whereas the absence of displacement is a characteristic of a DJ phase that is mostly based on bifunctional spacers.[20] LHPs can also be classified by the number *(n)* of the inorganic layers.[18,21,22] As n increases, the bandgap (E_g) decreases, and the system shifts toward the properties of 3D perovskites ($n = \infty$).[23] To this end, 3D FA-based perovskites are the most attractive materials in photovoltaics[10,24–26] since they are more thermally stable as compared to perovskite materials based on archetypical MA^+ central cations under device operation conditions.[26] Moreover, $FAPbI_3$ has a near-optimal band gap for light absorption, making it an ideal candidate for solar cells.[26] However, the perovskite α-$FAPbI_3$ phase is not thermodynamically stable below 150 °C and undergoes a phase transition to the photoinactive δ-$FAPbI_3$ phase.[24] Various methods have been developed for stabilizing the α-phase, such as intermixing with Cs^+ by optimizing the Goldschmidt tolerance factor due to its smaller ionic radius compared to FA^+, thereby promoting a more stable perovskite lattice.[24,27,28] This structural optimization alleviates lattice strain and enhances crystallinity while reducing defect density by promoting uniform grain growth.[1] Additionally, Cs^+, as an inorganic cation with a higher formation energy than organic counterparts like FA^+ or MA^+, enhances the thermal and environmental stability of the material. In 2D perovskites, Cs incorporation further improves crystallinity, promotes better phase orientation, and suppresses undesirable low-n phases that can hinder charge transport and device efficiency.[29,30] These effects collectively lead to higher phase purity and reduced nonradiative recombination, making Cs^+ particularly advantageous over other small monovalent cations such as Rb^+ or K^+, which are either too small or less compatible with the perovskite lattice.[29,31] Recent advancements in FA-based 2D perovskites highlighted the potential of both RP and DJ structures in achieving high power conversion efficiencies (PCEs) and enhanced stability. In RP systems, the incorporation of novel spacer cations has led to significant improvements. For instance, the use of β-fluorophenylethanamine (β-FPEA) as a spacer cation resulted in quasi-2D RP perovskites, with PCEs reaching 19.11%, attributed to enhanced crystallinity and optimized energy level alignment.[32] Similarly, selenophene-based spacers have been employed to achieve nominal $n = 5$ RP perovskites with PCEs exceeding 19%, demonstrating the effectiveness of spacer engineering in promoting higher-n phase formation.[33] However, direct structural confirmation of higher-n phases has been lacking. Similarly, in DJ perovskites, strategies such as seed-induced growth have been explored to control crystallization and phase distribution. A notable example involves the use of $MAPbCl_3$ and 1,4-butyldiammonium (BDA) based $BDAPbI_4$ as seeds to facilitate the growth of FA-based DJ perovskite films, leading to devices with PCEs of 20.0% and improved stability.[34] Another example is the 2D DJ perovskite solar cells achieving a PCE of 19.11% using $n = 5$ compositions.[35] This was attributed to the high efficiency and long-term stability due to a slight interlayer displacement that enhances charge transport and structural integrity. However, these studies lacked the structural confirmation of higher n-phase formation. The instability of α-$FAPbI_3$ is translated into the corresponding FA-based 2D perovskites, which demonstrated the incapacity to form higher-n phases ($n > 2$).[10,36,37] This was ascribed to the unfavorable enthalpies of formation, suggesting that the incorporation of smaller ions than Cs^+ could enable accessing higher-n ($n > 2$) phases of FA-based 2D perovskites, which remain unknown to date.

In this work, we investigate FA-based LHPs integrating benzylammonium (BNA)[38] and 1,4-phenylenedimethanammonium (PDMA) halides (X = I, Br; **Figure 1**) to explore the possibility of the formation of higher-n ($n > 2$) phases.[39] These organic spacers were chosen as representative model systems for RP (BNA) and DJ (PDMA) phases, respectively. The 2D perovskite structure was evidenced by X-ray diffraction (XRD) and solid-state nuclear magnetic resonance (NMR) spectroscopy, complemented by optoelectronic characterization using UV–vis absorption and photoluminescence (PL) spectroscopy, as well as their photovoltaic characteristics. The incorporation of Cs^+ into the perovskite framework was investigated by solid-state NMR spectroscopy, grazing incidence wide-angle X-ray scattering (GIWAXS) measurements, and density functional theory (DFT) calculations to identify the role of Cs^+ in the formation of higher ($n > 2$) compositional representatives, leading to a better understanding of the structure-property relationships that govern material characteristics and their application.

2. Results and Discussion

We synthesized FA-based LHPs by solution-processing (spin-coating) and mechanosynthesis, following the procedures detailed in the Experimental Section and the Supporting Information (Figures S1–S5, Supporting Information). We have analyzed $n = 1$–3 compositions of both RP and DJ phases based on different counter ions (X = I, Br), which were defined by the nominal (n) stoichiometry of the precursors without any assumptions about the structure of the resulting phase.[10] Their properties were analyzed by a combination of techniques to assess the formation of LHPs.

XRD measurements of thin films indicated the formation of FA-based LHPs (**Figure 2a,b**). The XRD patterns displayed diffraction peaks at low angles (below 10°) that correspond to low-dimensional perovskites in accordance with previous reports.[36,39] Moreover, a periodic pattern, typical of 2D perovskite structures oriented parallel to the substrates, was observed for $n = 1$ compositions, namely $(BNA)_2PbI_4$, $(PDMA)PbI_4$, $(BNA)_2PbBr_4$ and $(PDMA)PbBr_4$. For the iodide-based

---

N. Lempesis
Department of Chemistry
University of Ioannina
Ioannina 45110, Greece

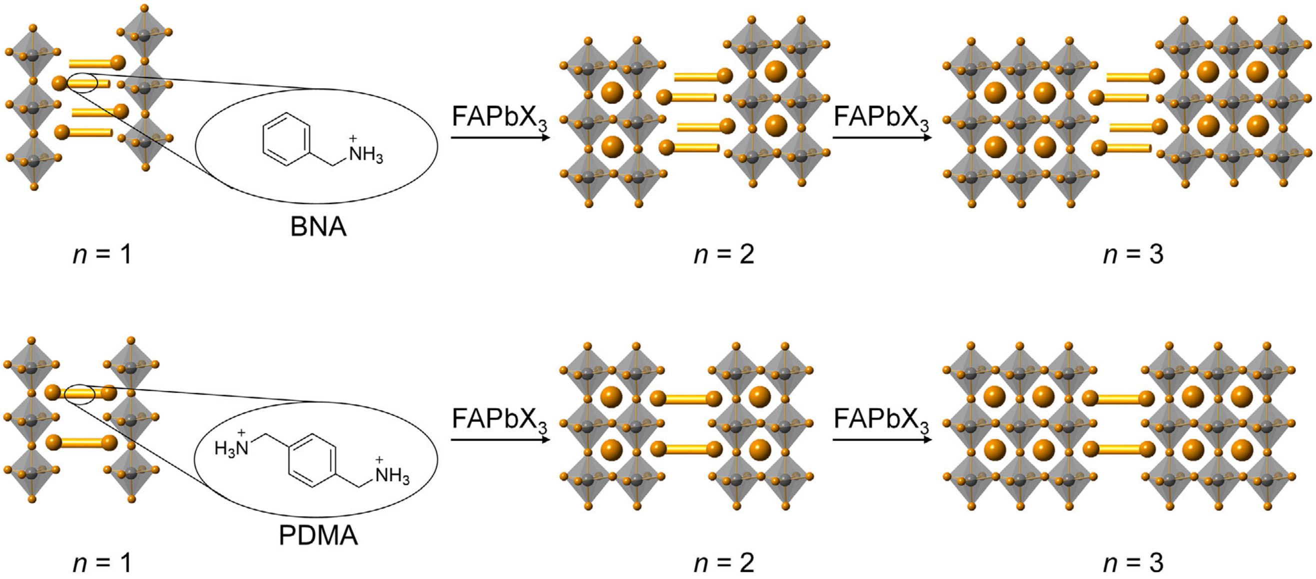

Figure 1. Layered hybrid halide perovskite (LHP) structure. Structural representation of benzylammonium (BNA) and 1,4- phenylenedimethanammonium (PDMA) based LHP systems (X = I, Br; FA = formamidinium) with the corresponding n = 1–3 phases.

$n = 2$ compositions ($(BNA)_2FAPb_2I_7$ and $(PDMA)FAPb_2I_7$), $n = 2$ phases were formed (indicated by the peaks at 4–5°) with co-existing $n = 1$ phases (at ≈6–7.3°) and 3D perovskite phases (at ≈14°). Such a mixture of phases is commonly observed for $n > 1$ compositions of 2D perovskites.[10] Bromide-based $(BNA)_2FAPb_2Br_7$ only showed peaks related to the $n = 1$ (≈5–7.5°) and 3D (≈14.8°) perovskite phases. Moreover, $n = 2$ compositions of PDMA-based perovskites showed lower intensity peaks below 10°, reflecting a decrease in the LHP yield or a change in the morphology[39,40]

The optoelectronic properties were thereafter analyzed by UV–vis absorption spectroscopy of the corresponding thin films. The $n = 1$ compositions revealed excitonic peaks that are typical for 2D perovskites at 510 nm in iodide-based compositions (Figure 2c),[40,41] whereas $n = 2$ nominal compositions displayed a gradual red shift of the absorption peaks in accordance with their lower bandgap.[23] The $n = 2$ compositions also featured additional signals that are likely associated with the co-existing $n = 1$ phases, along with an extended absorption reaching 800 nm, suggesting the presence of a 3D perovskite phase. This is typical for the behavior of higher n 2D perovskite thin films, where controlling phase purity remains a challenge.[23] Similarly, steady-state photoluminescence (PL) spectra of iodide-based systems (Figure 2c) showed well-defined emission peaks at ≈520 nm for $n = 1$ compositions, with a red shift for $n = 2$ systems. Moreover, the $n = 2$ compositions featured more significant Stokes shifts (>100 nm) that were previously associated with the presence of layered edge states (LESs) and co-existing 3D phases.[42] These shifts are also an indication of the presence of a mixture of phases.[10] In the case of the bromide-based samples, UV–vis absorption spectra (Figure 2d) showed excitonic peaks at ≈400 nm, corresponding to the $n = 1$ phase, whereas the $n = 2$ compositions exhibited additional signals indicative of higher n and 3D phases, which were smaller compared to the iodide-based samples. The PL spectra showed well-defined peaks at ≈410 nm for $n = 1$ compositions, with a red shift for $n = 2$ systems, featuring significant Stokes shifts similar to the iodide-based compositions. This is consistent with the XRD results, which predominantly showed $n = 1$ and 3D phases for the $n = 2$ nominal compositions.

The XRD peak assignment was further scrutinized by atomistic modeling. Structures corresponding to $n = 1$–3 phases for BNA and PDMA spacers were equilibrated and optimized at the DFT (PBE+Grimme D3 correction) level. The calculated XRD spectra for $n = 1$ and $n = 2$ compositions agreed with the experimental spectra, corroborating a mixture of $n = 1$ and $n = 2$ phases for the nominal $n = 2$ compositions (Figure S7, Supporting Information). The theoretical XRD spectra for $n = 3$ indicated a distinct peak at $2\theta = 3.2°$ for BNA and 3.4° for PDMA, which was not present in any measured spectra, suggesting the absence of $n = 3$ phases (Figure S7, Supporting Information). Similarly, the PL spectra of these samples (Figure 2c) did not show a significant difference between the $n = 1$ and $n = 2$ compositions, corroborating previous observations.

In summary, this analysis suggests that both BNA and PDMA spacers form LHP phases for $n = 1$ nominal composition in thin films of both iodide and bromide counter ions, whereas FA-based $n = 2$ compositions featured mixtures of phases, including $n = 1$ and 3D perovskite phases, which could not be controlled by the stoichiometry of the precursors. To better control this phase formation, especially for the increasing number of perovskite layers in $n > 1$ compositions, we investigated the role of Cs^+ incorporation into the perovskite framework.

2.1. Effect of Cs^+ Addition

To assess the effect of Cs^+ on the LHP phases, we fabricated and investigated $n = 2$–3 FA-based LHPs with a 5% Cs^+ content for both iodide and bromide-based perovskite compositions. The formation of the LHPs was analyzed by XRD (**Figure 3**a,b).

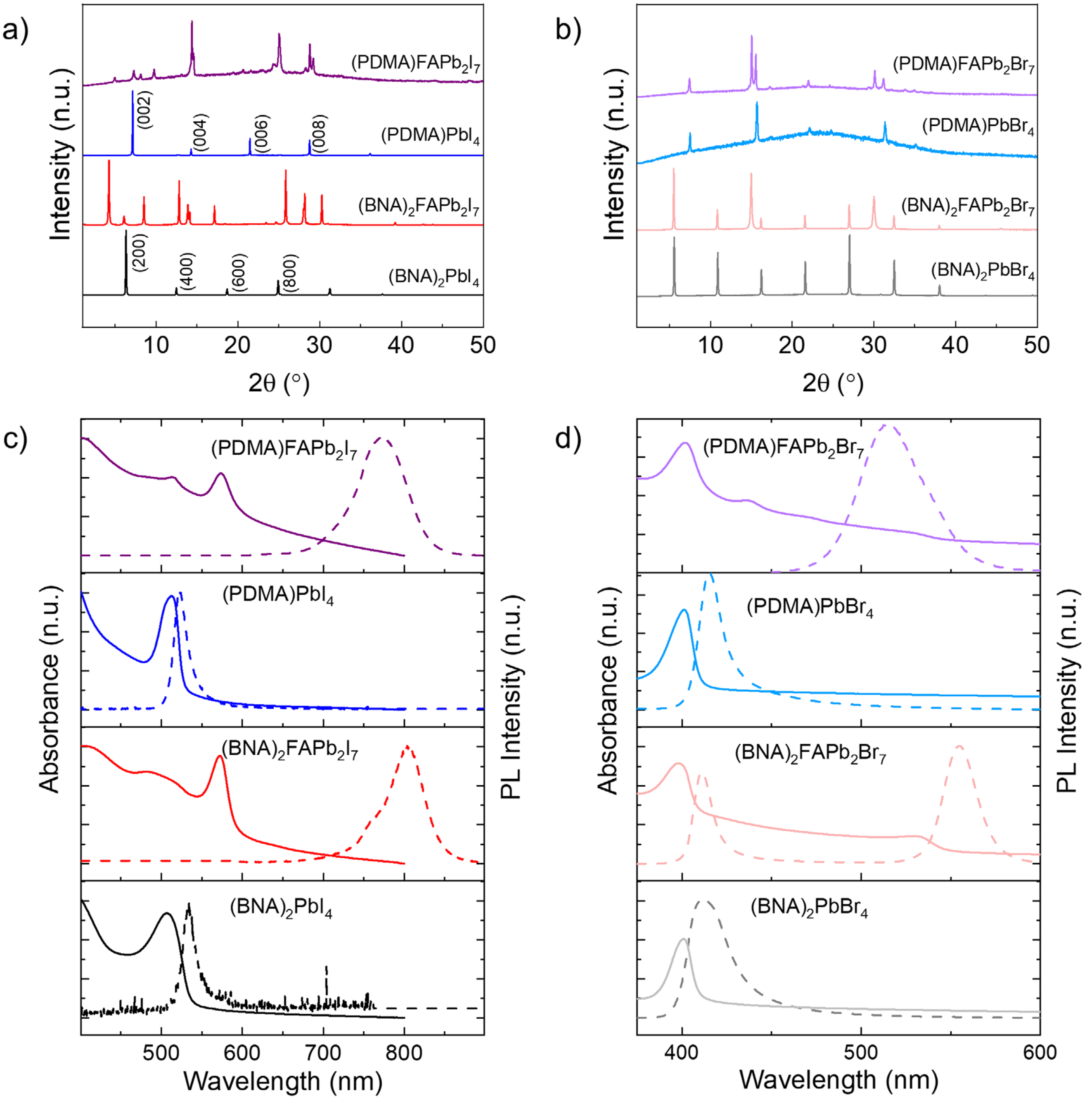

Figure 2. Formation of FA-based LHPs. a,b) XRD patterns of thin films on microscope glass for (a) $n = 1$ ($(BNA)_2PbI_4$ and $(PDMA)PbI_4$), and $n = 2$ ($(BNA)_2FAPb_2I_7$ and $(PDMA)FAPb_2I_7$) I-based samples, and (b) $n = 1$ ($(BNA)_2PbBr_4$ and $(PDMA)PbBr_4$), and $n = 2$ ($(BNA)_2FAPb_2Br_7$ and $(PDMA)FAPb_2Br_7$) Br-based samples. Optoelectronic properties based on c,d) UV–vis (full line) and PL (dashed line) spectra of films of $n = 1$ and $n = 2$ (c) I- and (d) Br-based compositions. The photographs of the films are shown in Figure S6 (Supporting Information).

All samples featured diffraction peaks below 10°, confirming the formation of low-dimensional perovskites. The XRD patterns for FA-based $n = 2$ and $n = 3$ compositions without Cs^+ were closely comparable, without any evidence of the presence of $n > 2$ phases. However, upon introducing Cs^+, changes were observed for $n = 3$ nominal compositions. Most of these peaks corresponded to the $n = 2$ phase and the 3D perovskite phase, which were in different ratios depending on the applied stoichiometry. The addition of Cs^+ alters the phase composition of the existing phases ($n = 1$, $n = 2$, and 3D perovskites) without the clear formation of the $n = 3$ phase. A new peak at 7.9° for the BNA-based sample was observed that could be related to the formation of a new phase. The new phases were further investigated through comparison with theoretical phase models. The XRD pattern for theoretical $n = 3$ structures predicted the same peak positions as for the case without Cs^+ at 3.23° for BNA and

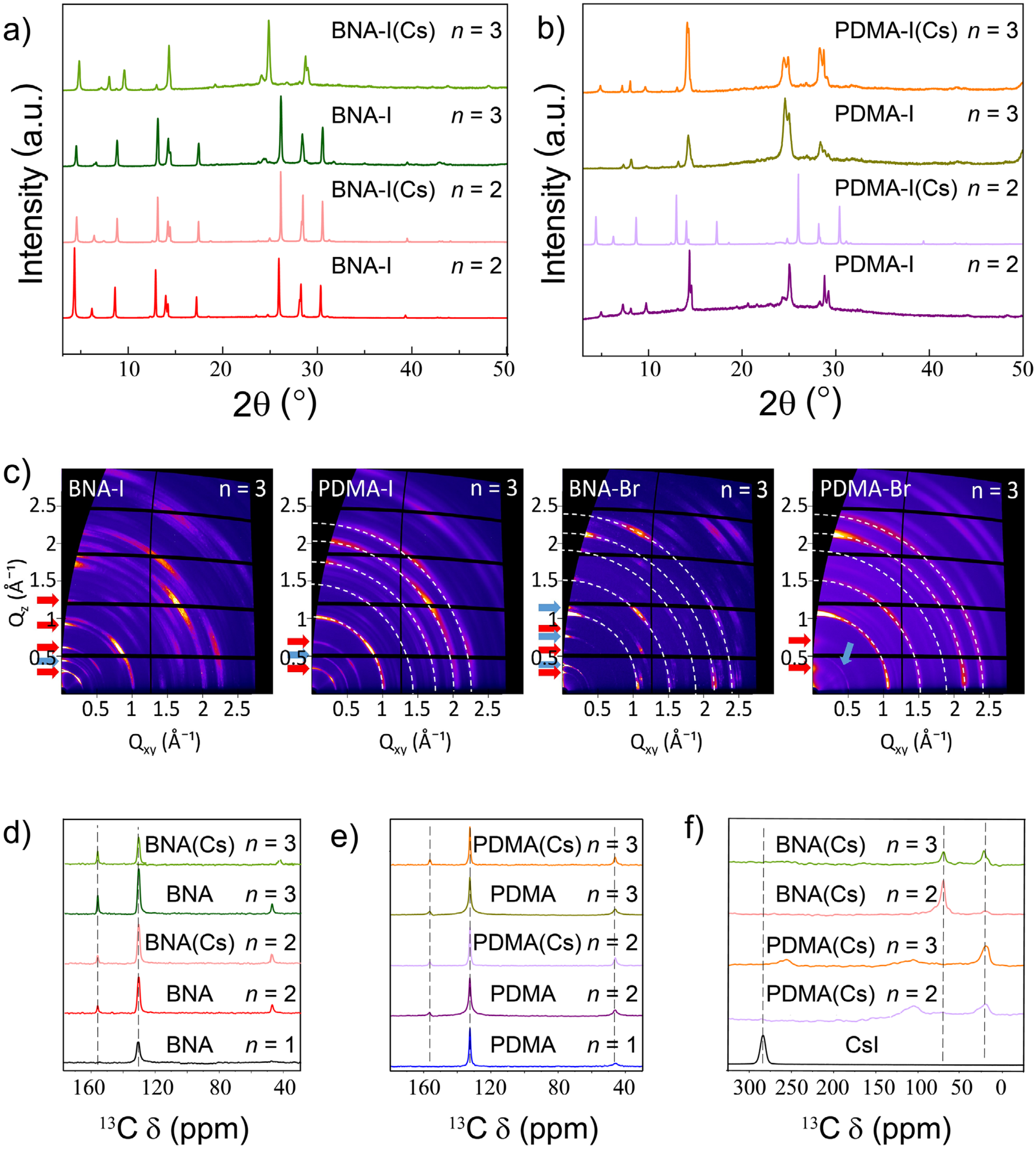

Figure 3. The effect of Cs^+ incorporation into FA-based LHPs. XRD patterns of $n = 2$ and $n = 3$ compositions of FA-based and Cs-containing thin films on microscope glass built upon a) BNA and b) PDMA iodides. XRD patterns for their bromide analogs are shown in Figure S11 (Supporting Information). c) GIWAXS reciprocal space maps at an incidence angle of 1°, for $n = 3$ compositions of $(BNA)_2(Cs_{0.05}FA_{0.95})_2Pb_3I_{10}$ (BNA-I), $(PDMA)(Cs_{0.05}FA_{0.95})_2Pb_3I_{10}$ (PDMA-I), $(BNA)_2(Cs_{0.05}FA_{0.95})_2Pb_3Br_{10}$ (BNA-Br), and $(PDMA)(Cs_{0.05}FA_{0.95})_2Pb_3Br_{10}$ (PDMA-Br) films. White dashed lines indicate signals for the perovskite phase, while colored arrows indicate $n = 1$ (blue) and $n = 2$ (red) phases. d,e) $^1H \rightarrow {}^{13}C$ cross-polarization (CP) magic angle spinning (MAS) NMR spectra of (d) $(BNA)_2FA_{n-1}Pb_nI_{3n+1}$ (BNA) and $(BNA)_2(Cs_{0.05}FA_{0.95})_{n-1}Pb_nI_{3n+1}$ (BNA(Cs)) and (e) $(PDMA)FA_{n-1}Pb_nI_{3n+1}$ (PDMA) and $(PDMA)(Cs_{0.05}FA_{0.95})_{n-1}Pb_nI_{3n+1}$ (PDMA(Cs)) based on $n = 1$–3 compositions. (f) ^{133}Cs NMR spectra for Cs-based perovskites compared to CsI. Vertical lines mark peak positions for $n = 2$–3 compositions.

3.4° for the PDMA-based samples (Figure S8, Supporting Information), which was not present in any measured datasets, suggesting the absence of $n =$ 3 phases in detectable amounts. The lowest angle peaks 4.7° and 9.4° for BNA and 4.3 and 8.7 for PDMA could be ascribed to the formation of the $n = 2$ phases, whereas the appearance of the new peak at 7.9° for the BNA spacer could be explained by the existence of a 1D phase (Figure S9, Supporting Information). A similar structure has previously been reported for benzo[c][1,2,5]thiadiazol-4-methylammonium (BTDZ) spacers,[43] which was supported by ab initio molecular dynamics (AIMD) simulations. The simulated XRD patterns for the 1D phase (Figure S10, Supporting Information) showed the lowest peak shifted by −0.3° compared to the experimentally observed peak at 7.9°. A similar deviation between simulated and experimental XRD patterns was also present for the $n = 2$ phases (Figures S7,S8, Supporting Information), which could be ascribed to the limited accuracy of the PBE functional with Grimme D3 correction[44] used to describe the system in the AIMD. For the bromide-based perovskites (Figure S11, Supporting Information), $(BNA)_2(Cs_{0.05}FA_{0.95})_2Pb_3Br_{10}$ exhibited the emergence of a peak at 4.03° that is attributed to the formation of $n = 2$ phase, while $(PDMA)(Cs_{0.05}FA_{0.95})Pb_2Br_7$ showed a high-intensity peak at 7.8° in addition to 30.4°, without indication of other low-dimensional phases.

This was further assessed by UV–vis absorption spectroscopy, revealing a blue shift in Cs-containing samples as compared to purely FA-based samples, which was more evident in the PDMA systems upon adding Cs^+ (Figures S12,S13, Supporting Information). In addition, a small shift of the absorption edge ≈800 nm was also observed for $n = 3$ PDMA samples, indicating the increase in the 3D perovskite contribution for $n > 1$ compositions. In the case of bromide-based compositions, a slight red shift was observed in Cs-containing BNA samples, while their PDMA-based DJ analogs also featured blue shifts in the presence of Cs^+ with more intense excitonic peaks. This was corroborated by the PL spectra, showing changes upon introducing Cs^+ with minor shifts and sharper signals, suggesting that Cs^+ might also affect phase purity. Specifically, new signals at ≈480 and ≈710 nm were observed upon adding Cs^+ in the iodide-based BNA systems, accompanied by a blue shift of the peak in the 780–805 nm range. On the contrary, for the bromide-based systems, almost no changes were observed upon adding Cs^+, leading us to focus our further investigation primarily on the iodide-based systems.

The formation of the $n = 3$ phase was also probed by grazing incidence wide-angle X-ray scattering (GIWAXS) for the nominal $n = 3$ compositions (Figure 3c). While $n = 1$ and $n = 2$ layered phases could be identified in the samples, in addition to 3D phases, there was no evidence of the formation of $n = 3$ LHP phases. Both $(BNA)_2(Cs_{0.05}FA_{0.95})_2Pb_3I_{10}$ and $(PDMA)(Cs_{0.05}FA_{0.95})_2Pb_3I_{10}$ layered phases exhibited two distinct preferred orientations for the direction of the layer stacking, i.e., vertically stacked and tilted by ≈36°. The main orientation for the stacking direction of $(BNA)_2(Cs_{0.05}FA_{0.95})_2Pb_3Br_{10}$ films was vertical, with a reduced degree of orientation for $(PDMA)(Cs_{0.05}FA_{0.95})_2Pb_3Br_{10}$ films (Figures S14,S15, Supporting Information). The peaks corresponding to the $n = 2$ phase were significantly broader than in other compositions, indicating a lower degree of crystallinity. While this investigation did not involve single-crystal X-ray structure analysis, it was complemented by additional experimental and theoretical insights to further clarify the underlying structural characteristics.

The structural characteristics were further assessed by solid-state NMR spectroscopy (Figure 3d–f), effective in inspecting atomic-level interactions.[45,46] For this purpose, powders of $(BNA)_2FA_{n-1}Pb_nI_{3n+1}$, $(PDMA)FA_{n-1}Pb_nI_{3n+1}$, $(BNA)_2(Cs_{0.05}FA_{0.95})_{n-1}Pb_nI_{3n+1}$ and $(PDMA)(Cs_{0.05}FA_{0.95})_{n-1}Pb_nI_{3n+1}$ ($n = 1$–3 compositions) were synthesized mechanosynthetically using ball milling (procedure reported in the Experimental Section). The ^{13}C NMR spectra showed small chemical shifts in the aromatic region (120 to 130 ppm) and the FA cation (150 to 160 ppm) for BNA-based systems (Figure 3d). Similarly, for the PDMA-based systems, minor shifts were observed in the $–CH_2–$ (40 to 50 ppm) and aromatic (130 to 140 ppm) regions, as well as for FA cations (150 to 160 ppm; Figure 3e), indicating the presence of the spacers and FA cations in a new structure or geometry. However, these changes were not sufficient to indicate the formation of $n = 3$ phase in the Cs-containing samples. ^{133}Cs NMR was applied to monitor the consumption of CsI (at ≈284 ppm) in all perovskite samples, which was accompanied by the appearance of a new peak at ≈22 ppm, suggesting the incorporation of Cs^+ into the structure.[45] However, the $n =$ 3 perovskite phase could not be unambiguously confirmed, corroborating the challenges in forming higher-n phases.

To understand the apparent absence of $n > 2$ phases, we relied on a theoretical investigation of the effect of different Cs^+ concentrations on the formation of higher-n phases by using AIMD simulations complemented by DFT calculations for a range of perovskite compositions ($n = 1$–3, the computational details are given in the Supporting Information). These results indicate that the formation energies for $n = 2$ remain lower than that of $n = 3$ compositions for any Cs^+ percentage less than 43% for BNA-based samples and ≈48% for PDMA-based ones (**Figure** 4), suggesting a threshold concentration for the formation of the $n = 3$ phase that was thereafter assessed experimentally.

To assess the effect of Cs^+ concentration on the resulting characteristics, samples incorporating different quantities of Cs^+ (15, 30, 45, 60, and 80%) were fabricated by spin-coating followed by annealing and investigated for their structural and optoelectronic properties. XRD was used to analyze the formation of the LHP phases (**Figure** 5a,b). While all samples exhibited low-angle reflection peaks below 10°, confirming the formation of low-dimensional perovskites, no additional peak ≈3° corresponding to a $n = 3$ phase was detected (according to the simulated XRD patterns in Figures S7,S8, Supporting Information), indicating the absence of this phase across all investigated Cs^+ concentrations. GIWAXS measurements (Figure S16, Supporting Information) revealed minor structural variations upon increasing the concentration of Cs^+ without the appearance of new signals. The BNA-based system was more oriented, especially the thin film containing 45% Cs^+ with spot-like diffraction patterns. At higher concentrations of Cs^+ (> 60%), minor changes could be observed in the XRD patterns, including the disappearance of the peaks at 9.9° and 28.3° along with the appearance of a new peak at 26.3° for the BNA-based sample, yet without unambiguously evidencing a distinct ($n = 3$) perovskite phase formation.

This was in accordance with the theoretical calculations, which showed the formation of competing 1D phases even at low

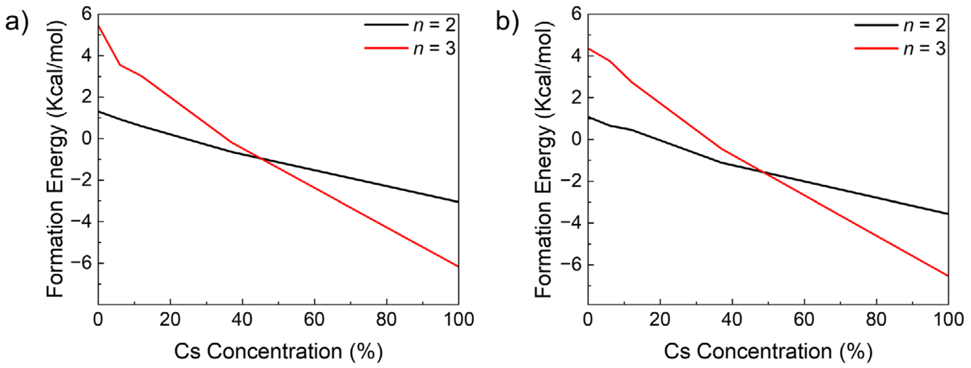

Figure 4. Factors governing the formation of higher-n phases in FA-based LHPs. Formation energies per stoichiometric unit for $n > 1$ LHP compositions compared to $n = 1$ based on a) BNA and b) PDMA iodide compositions.

concentrations of Cs$^+$, with lower formation energies than the $n = 3$ perovskite phase. In the $n = 3$ phase stoichiometry, it is possible to form two stoichiometric units of the 1D phase, i.e., (BNA)PbI$_3$, and a pure 3D phase of FAPbI$_3$. The estimated formation free energy of the 1D phase was lower than the formation free energy of the $n = 3$ phase, which points to the favoured formation of the 1D phase. Adding Cs$^+$ to the solution leads to a stabilisation of the 3D α-phase of FAPbI$_3$ and the 1D phase, which disfavours the formation of the $n = 3$ phase with increasing concentration of Cs$^+$ ions in the solution. This is accompanied by the emergence of the new XRD peaks ≈7° and the formation of the pure Cs$^+$ phases, such as the δ-CsPbI$_3$ phase with a characteristic XRD peak at 10° (Figure S17, Supporting Information). The new emerging peak at 7.9° at low Cs$^+$ concentration could be ascribed to a 1D phase based on the δ-FAPbI$_3$, with FA$^+$ replaced by the larger BNA spacer ion (Figure S10, Supporting Information). On the other hand, the peak at 7° present at high Cs$^+$ concentration could be assigned to the 1D phase based on the δ-CsPbI$_3$ phase with the Cs$^+$ replaced by the BNA spacer (Figure S17, Supporting Information). At intermediate Cs$^+$ concentrations between 15–45%, a peak at 7.4° emerges, with the highest intensity at 30% of Cs$^+$, corresponding to a real-space distance of 11.9 Å between diffraction planes. This is too large for any 3D phase or the iodide salts of precursors, yet smaller than the values corresponding to 2D phases, and requires further analysis to be adequately identified beyond the scope of this study. Nonetheless, even if the $n = 3$ becomes more stable than the $n = 2$ phase with increasing concentration of Cs$^+$, its formation was not observed due to the formation of a variety of competing low-dimensional or segregated phases with lower formation energies.

These changes were reflected in the optical properties (Figure 5c,d). UV–vis absorption spectra revealed nearly identical peaks in the 570–575 nm range for all the BNA-based samples, with a slight blue shift for this peak as the Cs$^+$ concentration increases. In the PDMA-based system, a main peak ≈565 nm was observed corresponding to the $n = 2$ phase, which also shows a slight blue shift with the increase in Cs$^+$ concentration; however, a new red-shifted peak in the range of 610–620 nm emerged for the samples having Cs$^+$ percentage equal to or higher than 30%, which was theoretically predicted for higher n-phases, in accordance with the PL spectra. While some of these spectral changes could be associated with the formation of new phases, PXRD and GIWAXS data do not support the assumption that $n = 3$ phase forms in the presence of Cs$^+$ in sufficient quantities to be detected. This shift could, therefore, be due to the formation of other Cs-containing phases with higher Cs$^+$ concentrations, such as other low-dimensional Cs-containing phases, more likely to form under these conditions.

The impact of Cs$^+$ addition on the optoelectronic properties was further evaluated in solar cell devices. These devices were n-i-p perovskite solar cells with a fluorine-doped tin oxide (FTO)/compact titanium dioxide (c-TiO$_2$)/mesoporous TiO$_2$ (m-TiO$_2$)/perovskite/2,2′,7,7′-tetrakis (*N*,*N*-di-4-methoxyphenylamino)-9,9′-spirobifluorene (spiro-OMeTAD)/gold (Au) architecture, featuring an active area of 0.16 cm^2 (0.4 cm × 0.4 cm). The $J-V$ characteristics of the perovskite solar cells were recorded under standard AM1.5 illumination with a light intensity of 100 mW cm^{-2} (Figures S18,S19, Supporting Information). An enhancement in the photovoltaics properties is observed upon the addition of Cs$^+$, with PCE of champion devices increasing from 6.1% for (BNA)$_2$FA$_2$Pb$_3$I$_{10}$ to 7.2% for (BNA)$_2$(Cs$_{0.05}$FA$_{0.95}$)$_2$Pb$_3$I$_{10}$. Similarly, for the PDMA-I based devices, there is an enhancement in the PCE of the champion devices from 4.5% for (PDMA)FA$_2$Pb$_3$I$_{10}$ to 5.7% for (PDMA)(Cs$_{0.05}$FA$_{0.95}$)$_2$Pb$_3$I$_{10}$. This increase was accompanied by an increase in the average current density (J_{sc}), fill factor (FF), and open circuit voltage (V_{oc}) upon the addition of Cs$^+$ for both sets of devices. The integrated current density, derived from the internal photon conversion efficiency (IPCE) spectra, and the short-circuit J_{sc} values obtained from the current–voltage characteristics were measured for the devices (Figure S20, Supporting Information). In the case of BNA-based devices (Figure S20a, Supporting Information), BNA-I(Cs) exhibited consistently higher IPCE values across the spectrum, leading to an integrated J_{sc} of ≈11.7 mA cm^{-2}, compared to ≈10.1 mA cm^{-2} for BNA-I. For the PDMA-based devices (Figure S20b, Supporting Information), a similar trend is observed, with PDMA-I(Cs) showing broader spectral response and a modest increase in integrated J_{sc} (≈8.6 mA cm^{-2} compared to ≈7.4 mA cm^{-2}). While the overall performance can be further optimized in functional devices, which goes beyond the scope of this study, the enhancement upon Cs$^+$ addition can be attributed to factors other than the formation of higher-n phases, including

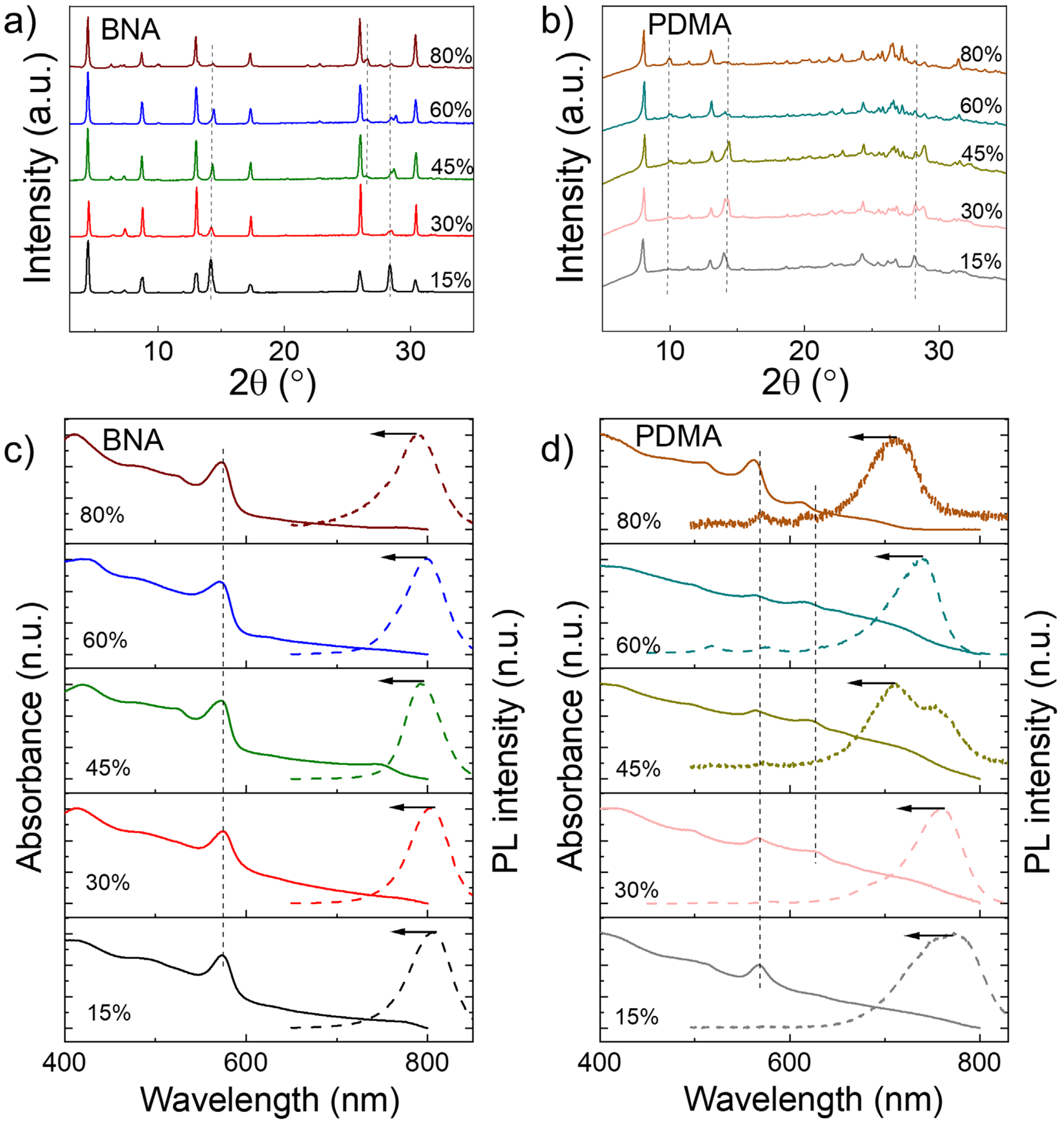

Figure 5. Identifying critical Cs$^+$ concentration for FA-based LHP phases. a,b) XRD patterns of $n = 3$ FACs-containing thin films incorporating different Cs$^+$ percentages on glass for systems based on (a) BNA and (b) PDMA iodide with their c,d) UV–vis and PL spectra. The black arrows indicate shifts of the emission with increasing Cs$^+$ concentration.

the stabilization of the 3D α-FAPbI$_3$ phase, crystal orientation, morphology, and surface quality,[29,47,48] contributing to the overall performance. This broadens the understanding of the stabilization of FA-based low-dimensional perovskite phases, stimulating further investigations.

To evaluate the impact of Cs$^+$ on film morphology, plane-view scanning electron microscopy (SEM) images of the films were obtained (Figure S21, Supporting Information). The BNA-I films without Cs$^+$ showed poor surface coverage with non-uniform grains and pinholes, while the BNA-I(Cs) film demonstrated improved uniformity and compactness. Similarly, PDMA-I films exhibited increased grain size and clearer grain boundaries upon Cs$^+$ incorporation, indicating enhanced crystal growth and film quality. These morphological improvements correlate well with the improved photovoltaic performance of Cs^+ containing devices.

The use of Cs^+ was also expected to influence the operational stability of the perovskite solar cells. To evaluate this, we monitored the photovoltaic performance at the maximum power point (MPP) under continuous illumination in an inert atmosphere at ambient temperature (Figure S22, Supporting Information). Notably, the devices had been aged for over two months prior to testing, which provides a more stringent assessment of their operational durability. While overall stability may be considered modest due to aging, the Cs-containing samples clearly demonstrated improved operational stability compared to their Cs-free counterparts. This enhancement is attributed to the stabilizing effect of Cs^+ on the 3D perovskite lattice as reported previously.[25,49] These findings demonstrate the beneficial effect of the Cs^+ addition in improving the operational stability of perovskite solar cells.

3. Conclusion

A systematic examination of layered hybrid perovskites based on $(BNA)_2(FA_xCs_y)_{n-1}Pb_nI_{3n+1}$ and $(PDMA)(FA_xCs_y)_{n-1}Pb_nI_{3n+1}$ ($n = 1$–3) compositions was performed to understand the impact of incorporating Cs^+ on the formation of higher n-phases. While 5% Cs^+ incorporation into the perovskite framework induced minor changes in the structural and optoelectronic characteristics, we found no evidence for the formation of the $n = 3$ phase. X-ray scattering measurements indicated a mixture of $n = 1$, $n = 2$, and 3D phases in the $n = 3$ compositions, with the absence of the $n = 3$ phase. Molecular dynamics simulations and density functional theory calculations suggested this was due to unfavorable formation enthalpies, which were estimated to be beneficial only in higher Cs^+ concentrations (> 40%) for both BNA and PDMA-based LHP materials. While thin films with a high Cs^+ percentage show some difference in their structural properties with preferential formation of $n = 2$ phase for the BNA-Br samples in the presence of Cs^+, the formation of higher-n phases could not be unambiguously identified under these conditions. Instead, theoretical analysis suggests the preferential formation of other low-dimensional phases. Nonetheless, incorporating small amounts of Cs^+ (5%) into the perovskite material led to improvements in the photovoltaic characteristics. This provides important insights into the design of FA-based LHPs and the factors governing their structural and optoelectronic properties. While the use of FA-based mixed-dimensional perovskite compositions is of increasing interest for photovoltaics, our investigation suggests that this is not likely to involve the formation of 2D perovskites other than $n = 1$–2 phases. These findings have a broader implication for the design and application of FA-based LHPs in optoelectronics.

Supporting Information

Supporting Information is available from the Wiley Online Library or from the author.

Acknowledgements

G.A. and J.V.M. acknowledge funding from the Swiss National Science Foundation project no. 193174. The authors also appreciate the support and mentorship of Prof. Ullrich Steiner (Adolphe Merkle Institute), Prof. Kevin Sivula (EPFL), and Dr. Lukas Pfeifer (EPFL) throughout the project. U.R. acknowledges funding from the Swiss National Science Foundation under grant No. 200020_219440 and computational resources from the Swiss National Computing Center CSCS. D.J.K. acknowledges the ERC Starting Grant PhotoPeroNMR project funded by UKRI Horizon Europe guarantee (EP/Y01376X/1). The solid-state NMR experiments in this work were carried out through the European project PANACEA, which has received funding from the European Union's Horizon 2020 research and innovation programme under Grant Agreement No 101008500. The authors also thank the BMBF for supporting project 05K19VTA (ERUM-Pro). The authors acknowledge DESY (Hamburg, Germany), a member of the Helmholtz Association HGF, for the provision of experimental facilities. Parts of this research were carried out at PETRA III. Beamtime was allocated for proposal I-20220258. The authors thank Azat Khadiev and Dmitri Novikov for assistance in using beamline P23. M.A. gratefully acknowledges King Abdulaziz City for Science and Technology (KACST) for the fellowship. The authors are grateful for the invaluable support of Dr. Shaik Mohammed Zakeeruddin (EPFL) throughout the project.

Conflict of Interest

The authors declare no conflict of interest.

Author Contributions

The project was conceptualised by J.V.M. and led by G.A., who conducted molecular synthesis (with the support of Dr. Lukas Pfeifer at EPFL) and characterization, as well as thin film and device fabrication and characterisation with the support of M.A. Throughout the study, V.S., V.C., N.L. and L.A. performed theoretical investigations under the supervision of U.R. who also contributed to their interpretation, whereas G.A. conducted the solid-state NMR spectroscopy with the support of L.P. In addition, P.A.S. conducted part of the GIWAXS measurements and analysis independently, whereas L.M., P.Z., and A.H. carried out another part of GIWAXS measurements under the supervision of F.S. The project was managed by M.G. and J.V.M. All authors contributed to the manuscript.

Data Availability Statement

Data presented here can be accessed at the following DOI:10.5281/zenodo.15722103, and it is available under the license CC-BY-4.0 (Creative Commons Attribution-ShareAlike 4.0 International).

Keywords

Cs doping, FA-based 2D perovskites, layered hybrid perovskites, optoelectronics

Received: March 4, 2025
Revised: June 9, 2025
Published online: July 4, 2025

---

[1] M. Saliba, T. Matsui, J.-Y. Seo, K. Domanski, J.-P. Correa-Baena, M. K. Nazeeruddin, S. M. Zakeeruddin, W. Tress, A. Abate, A. Hagfeldt, *Energy Environ. Sci.* **2016**, *9*, 1989.
[2] A. K. Jena, A. Kulkarni, T. Miyasaka, *Chem. Rev.* **2019**, *119*, 3036.
[3] M. Grätzel, *Acc. Chem. Res.* **2017**, *50*, 487.
[4] Y. Zhao, K. Zhu, *Chem. Soc. Rev.* **2016**, *45*, 655.
[5] M. H. Futscher, J. V. Milić, *Front. Energy Res.* **2021**, *9*, 629074.

[6] J. Wei, Q. Wang, J. Huo, F. Gao, Z. Gan, Q. Zhao, H. Li, *Adv. Energy Mater.* **2021**, *11*, 2002326.

[7] J.-P. Correa-Baena, M. Saliba, T. Buonassisi, M. Grätzel, A. Abate, W. Tress, A. Hagfeldt, *Science* **2017**, *358*, 739.

[8] Y. Rong, Y. Hu, A. Mei, H. Tan, M. I. Saidaminov, S. I. Seok, M. D. McGehee, E. H. Sargent, H. Han, *Science* **2018**, *361*, aat8235.

[9] G. Grancini, M. K. Nazeeruddin, *Nat. Rev. Mater.* **2019**, *4*, 4.

[10] J. V. Milić, S. M. Zakeeruddin, M. Grätzel, *Acc. Chem. Res.* **2021**, *54*, 2729.

[11] J. Even, M. Kepenekian, G. Volonakis, L. Pedesseau, S. Thébaud, M. Zacharias, W. Li, M. G. Kanatzidis, A. D. Mohite, C. Katan, in MRS Fall 2023 **2023**.

[12] W. A. Dunlap-Shohl, Y. Zhou, N. P. Padture, D. B. Mitzi, *Chem. Rev.* **2019**, *119*, 3193.

[13] D. B. Mitzi, *Inorg. Chem.* **2000**, *39*, 6107.

[14] D. B. Mitzi, *J. Chem. Soc. Dalton Trans.* **2001**, 1.

[15] D. B. Mitzi, *J. Solid State Chem.* **1999**, *145*, 694.

[16] A. Dučinskas, M. Jung, Y.-R. Wang, J. V. Milić, D. Moia, M. Grätzel, J. Maier, *J. Mater. Chem. C* **2024**, *12*, 7909.

[17] J. S. Manser, J. A. Christians, P. V. Kamat, *Chem. Rev.* **2016**, *116*, 12956.

[18] L. Mao, C. C. Stoumpos, M. G. Kanatzidis, *J. Am. Chem. Soc.* **2019**, *141*, 1171.

[19] C. C. Stoumpos, D. H. Cao, D. J. Clark, J. Young, J. M. Rondinelli, J. I. Jang, J. T. Hupp, M. G. Kanatzidis, *Chem. Mater.* **2016**, *28*, 2852.

[20] L. Mao, W. Ke, L. Pedesseau, Y. Wu, C. Katan, J. Even, M. R. Wasielewski, C. C. Stoumpos, M. G. Kanatzidis, *J. Am. Chem. Soc.* **2018**, *140*, 3775.

[21] M. E. Kamminga, H.-H. Fang, M. R. Filip, F. Giustino, J. Baas, G. R. Blake, M. A. Loi, T. T. M. Palstra, *Chem. Mater.* **2016**, *28*, 4554.

[22] M. Kepenekian, B. Traore, J.-C. Blancon, L. Pedesseau, H. Tsai, W. Nie, C. C. Stoumpos, M. G. Kanatzidis, J. Even, A. D. Mohite, S. Tretiak, C. Katan, *Nano Lett.* **2018**, *18*, 5603.

[23] J. V. Milić, J.-H. Im, D. J. Kubicki, A. Ummadisingu, J.-Y. Seo, Y. Li, M. A. Ruiz-Preciado, M. I. Dar, S. M. Zakeeruddin, L. Emsley, M. Grätzel, *Adv. Energy Mater.* **2019**, *9*, 1900284.

[24] Z. Li, M. Yang, J. S. Park, S. H. Wei, J. J. Berry, K. Zhu, *Chem. Mater.* **2016**, *28*, 284.

[25] G. E. Eperon, S. D. Stranks, C. Menelaou, M. B. Johnston, L. M. Herz, H. J. Snaith, *Energy Environ. Sci.* **2014**, *7*, 982.

[26] A. Binek, F. C. Hanusch, P. Docampo, T. Bein, *J. Phys. Chem. Lett.* **2015**, *6*, 1249.

[27] D. Bi, X. Li, J. V. Milić, D. J. Kubicki, N. Pellet, J. Luo, T. LaGrange, P. Mettraux, L. Emsley, S. M. Zakeeruddin, M. Grätzel, *Nat. Commun.* **2018**, *9*, 4482.

[28] S.-H. Turren-Cruz, A. Hagfeldt, M. Saliba, *Science* **2018**, *362*, 449.

[29] X. Zhang, X. Ren, B. Liu, R. Munir, X. Zhu, D. Yang, J. Li, Y. Liu, D.-M. Smilgies, R. Li, *Energy Environ. Sci.* **2017**, *10*, 2095.

[30] S. Ahmad, R. Lu, Y. Liu, X. Liu, Q. Yang, X. Guo, C. Li, *Nano Energy* **2022**, *103*, 107822.

[31] M. Jain, B. Fasnick CK, M. Khemnani, L. Kortstee, B. Andola, M. J. Patel, A. Guerrero, Y. K. Srivastava, I. E. Castelli, A. Solanki, *Nano Energy* **2025**, *138*, 110871.

[32] Y. Zhang, M. Chen, T. He, H. Chen, Z. Zhang, H. Wang, H. Lu, Q. Ling, Z. Hu, Y. Liu, Y. Chen, G. Long, *Adv. Mater.* **2023**, *35*, 2210836.

[33] Q. Fu, M. Chen, Q. Li, H. Liu, R. Wang, Y. Liu, *J. Am. Chem. Soc.* **2023**, *145*, 21687.

[34] G. Wu, T. Liu, M. Hu, Z. Zhang, S. Li, L. Xiao, J. Guo, Y. Wang, A. Zhu, W. Li, H. Zhou, Y. Zhang, R. Chen, G. Xing, *Adv. Mater.* **2023**, *35*, 2303061.

[35] W. Zhang, Z. Liu, L. Zhang, H. Wang, C. Jiang, X. Wu, C. Li, S. Yue, R. Yang, H. Zhang, J. Zhang, X. Liu, Y. Zhang, H. Zhou, *Nat. Commun.* **2024**, *15*, 5709.

[36] M. C. Gélvez-Rueda, P. Ahlawat, L. Merten, F. Jahanbakhshi, M. Mladenović, A. Hinderhofer, M. I. Dar, Y. Li, A. Dučinskas, B. Carlsen, W. Tress, A. Ummadisingu, S. M. Zakeeruddin, F. Schreiber, A. Hagfeldt, U. Rothlisberger, F. C. Grozema, J. V. Milić, M. Graetzel, *Adv. Funct. Mater.* **2020**, *30*, 2003428.

[37] F. Jahanbakhshi, M. Mladenović, E. Kneschaurek, L. Merten, M. C. Gélvez-Rueda, P. Ahlawat, Y. Li, A. Dučinskas, A. Hinderhofer, M. I. Dar, W. Tress, B. Carlsen, A. Ummadisingu, S. M. Zakeeruddin, A. Hagfeldt, F. Schreiber, F. C. Grozema, U. Rothlisberger, J. V. Milić, M. Graetzel, *J. Mater. Chem. A* **2020**, *8*, 17732.

[38] F. Wang, W. Geng, Y. Zhou, H.-H. Fang, C.-J. Tong, M. A. Loi, L.-M. Liu, N. Zhao, *Adv. Mater.* **2016**, *28*, 9986.

[39] Y. Li, J. V. Milić, A. Ummadisingu, J.-Y. Seo, J.-H. Im, H.-S. Kim, Y. Liu, M. I. Dar, S. M. Zakeeruddin, P. Wang, A. Hagfeldt, M. Grätzel, *Nano Lett.* **2019**, *19*, 150.

[40] H. Tsai, W. Nie, J.-C. Blancon, C. C. Stoumpos, R. Asadpour, B. Harutyunyan, A. J. Neukirch, R. Verduzco, J. J. Crochet, S. Tretiak, L. Pedesseau, J. Even, M. A. Alam, G. Gupta, J. Lou, P. M. Ajayan, M. J. Bedzyk, M. G. Kanatzidis, A. D. Mohite, *Nature* **2016**, *536*, 312.

[41] D. H. Cao, C. C. Stoumpos, O. K. Farha, J. T. Hupp, M. G. Kanatzidis, *J. Am. Chem. Soc.* **2015**, *137*, 7843.

[42] J.-C. Blancon, H. Tsai, W. Nie, C. C. Stoumpos, L. Pedesseau, C. Katan, M. Kepenekian, C. M. M. Soe, K. Appavoo, M. Y. Sfeir, S. Tretiak, P. M. Ajayan, M. G. Kanatzidis, J. Even, J. J. Crochet, A. D. Mohite, *Science* **2017**, *355*, 1288.

[43] W. Luo, S. Kim, N. Lempesis, L. Merten, E. Kneschaurek, M. Dankl, V. Carnevali, L. Agosta, V. Slama, Z. VanOrman, *Adv. Sci.* **2024**, *11*, 2405622.

[44] S. Grimme, *J. Comput. Chem.* **2006**, *27*, 1787.

[45] D. J. Kubicki, D. Prochowicz, A. Hofstetter, S. M. Zakeeruddin, M. Grätzel, L. Emsley, *J. Am. Chem. Soc.* **2017**, *139*, 14173.

[46] A. Q. Alanazi, M. H. Almalki, A. Mishra, D. J. Kubicki, Z. Wang, L. Merten, F. T. Eickemeyer, H. Zhang, D. Ren, A. Y. Alyamani, H. Albrithen, A. Albadri, M. H. Alotaibi, A. Hinderhofer, S. M. Zakeeruddin, F. Schreiber, A. Hagfeldt, L. Emsley, J. V. Milić, M. Graetzel, *Adv. Funct. Mater.* **2021**, *31*, 2101163.

[47] C. Yi, J. Luo, S. Meloni, A. Boziki, N. Ashari-Astani, C. Grätzel, S. M. Zakeeruddin, U. Röthlisberger, M. Grätzel, *Energy Environ. Sci.* **2016**, *9*, 656.

[48] D. P. McMeekin, G. Sadoughi, W. Rehman, G. E. Eperon, M. Saliba, M. T. Hörantner, A. Haghighirad, N. Sakai, L. Korte, B. Rech, *Science* **2016**, *351*, 151.

[49] X. Liu, M. Chen, Y. Zhang, J. Xia, J. Yin, M. Li, K. G. Brooks, R. Hu, X. Gao, Y.-H. Kim, A. Züttel, J. M. Luther, S. Kinge, Y. Feng, M. K. Nazeeruddin, *Chem. Eng. J.* **2022**, *431*, 133713.